Bound and unbound substructures in Galaxy-scale Dark Matter haloes

Michal Maciejewski[1*] , Mark Vogelsberger[1,2], Simon D.M. White[1],
Volker Springel[1,3]

[1] *Max-Planck-Institut für Astrophysik, Garching, Karl-Schwarzschild-Straße 1, 85741 Garching bei München, Germany*
[2] *Harvard-Smithsonian Center for Astrophysics, 60 Garden Street, Cambridge, MA 02138, USA*
[3] *Heidelberg Institute for Theoretical Studies, Schloss-Wolfsbrunnenweg 35, D-69118 Heidelberg, Germany*

14 October 2010

ABSTRACT

We analyse the coarse-grained phase-space structure of the six Galaxy-scale dark matter haloes of the Aquarius Project using a state-of-the-art 6D substructure finder. Within r_{50}, we find that about 35% of the mass is in identifiable substructures, predominantly tidal streams, but including about 14% in self-bound subhaloes. The slope of the differential substructure mass function is close to -2, which should be compared to ~ -1.9 for the population of self-bound subhaloes. Near r_{50} about 60% of the mass is in substructures, with about 30% in self-bound subhaloes. The inner 35 kpc of the highest resolution simulation has only 0.5% of its mass in self-bound subhaloes, but 3.3% in detected substructure, again primarily tidal streams. The densest tidal streams near the solar position have a 3-D mass density about 1% of the local mean, and populate the high velocity tail of the velocity distribution.

Key words: methods: numerical, cosmology: dark matter

1 INTRODUCTION

The detailed phase-space distribution of cold dark matter haloes can substantially affect prospects for dark matter detection. Direct detection experiments are starting to probe significant fractions of the parameter space of plausible theoretical models, so a first detection of dark matter (DM) may be imminent. Only recently has realistic prediction of the phase-space structure near the Earth become possible, because very high-resolution numerical simulations are required. It is now well established that the outer regions of cold dark matter (CDM) haloes have a complicated phase-space structure with many subhaloes and tidal streams (Moore et al. 1999; Klypin et al. 1999; Ghigna et al. 2000; Stoehr et al. 2002; Diemand et al. 2004, 2008; Springel et al. 2008). This raises the question of whether similar structures might affect direct detection probabilities. Could the Earth be sitting in a "hole", i.e. a locally very underdense region, in the DM distribution, as might occur in a fractal structure, or if most of the mass near the Sun were concentrated in dense, low-mass subhaloes. Some simulators have indeed argued that a significant fraction of the local mass could lie in solar or Earth-mass sub-

haloes (e.g. Diemand et al. 2005), although more recent simulations suggest that the local mass fraction in bound subhaloes of any mass is well below 1% (Vogelsberger et al. 2009; Vogelsberger & White 2010). Other possibilities might be for the Earth to lie within a subhalo, or within a dense tidal stream created by disruption of an earlier subhalo. Either of these would produce a spike in the velocity distribution of local dark matter particles.

Quantifying the detailed phase-space structure of a halo requires disentangling its various DM components: the smooth component which is, in fact, a superposition of many fundamental streams (Vogelsberger & White 2010); compact, self-bound subhaloes; and tidal streams created by the disruption of such subhaloes. Efficient identification of the tidal streams requires a sensitive and robust structure-finder in 6D phase-space. Recently Maciejewski et al. (2009a) presented an algorithm, Hierarchical Structure Finder (HSF), designed specifically for this purpose. HSF identifies structures in an N-body simulation as coherent, overdense sets of particles in the full 6D position-velocity distribution. In this paper we use HSF to study the six Galaxy-scale halos simulated as part of the Aquarius Project (Springel et al. 2008), providing a quantitative analysis of the various halo components and focussing, in particular, on the inner halo relevant for detection experiments.

---

* E-mail: michalm@mpa-garching.mpg.de

Our paper is organised as follows: Section 2 presents a brief description of our Hierarchical Structure Finder. Section 3 then explores the numerical convergence of our results by analysing simulations of a single halo at a variety of resolutions. Finally we use the full set of six Aquarius halos to study the expected scatter in substructure properties among Galaxy-scale halos. Section 4 focusses on substructure in the inner halo in order to assess possible consequences for direct detection experiments. The final section gives our conclusions.

2   HIERARCHICAL STRUCTURE FINDER

Many different algorithms for identifying (sub)structure have been applied to N-body simulations of the growth of cosmic structure. One of the first and most widely used is the Friends-of-Friends (FOF) scheme introduced by Davis et al. (1985); this defines "halos" as disjoint particle sets containing every particle closer than some maximal linking length to at least one other member of its set. This bounds objects approximately by an isodensity surface, but makes no assumption about their shape or internal structure. In contrast, the Spherical Overdensity (SO) group-finder of Cole & Lacey (1996) finds high-density peaks in the particle distribution, grows spheres centred on each until the mean enclosed density drops to a specified value (typically ~ 200 times the cosmological mean) and then defines halos as the contents of those spheres whose centres do not lie within a more massive halo. More recent structure-finders [e.g. SKID (Governato et al. 1997), SUBFIND (Springel et al. 2001), VOBOZ (Neyrinck et al. 2005), PSB (Kim & Park 2006), ADAPTAHOP (Aubert, Pichon & Colombi 2004), AHF (Knollmann & Knebe 2010), HSF (Maciejewski et al. 2009a)] typically identify objects as connected self-bound particle sets above some density threshold. Such methods have two steps. Each particle is first linked to a local DM density maximum by following the gradient of a particle-based estimate of the underlying DM density field. The particle set attached to a given maximum defines a candidate structure. In a second step, particles which are gravitationally unbound to the structure are discarded until a fully self-bound final object is obtained. The various methods differ in the way particles are treated when they belong to more than one candidate and in the way unbound particles are redistributed. Most methods produce a hierarchical characterisation of structure where halos contain subhaloes which in turn can contain their own subhaloes.

These methods can be extended to higher dimensions, in particular to 6D phase-space. The main complication is then that the smoothed density field and its gradient must be estimated from the particle distribution in six dimensions. The Hierarchichal Structure Finder (HSF) presented by Maciejewski et al. (2009a) is an algorithm of this type, and can be used, just like the above 3D algorithms, to identify bound subhaloes. Other six dimensional phase-space structure finders have been developed recently by Diemand et al. (2006, 6dFOF) and Sharma & Johnston (2009, EnLink). In the following we describe the HSF method in somewhat more detail, since this is the method we will use for the rest of this paper. Further technical details and tests can be found in Maciejewski et al. (2009a).

To find candidate structures we first need to estimate phase-space densities at the positions of all the particles. Furthermore we need to calculate local phase-space density gradients. HSF does this using a six-dimensional SPH smoothing kernel with a local adaptive metric as implemented in the EnBiD code (Sharma & Steinmetz 2006). Neighbouring particles can then be used to derive the required gradients. For the SPH kernel we use $N_{\mathrm{sph}} = 64$ neighbours whereas for the gradient estimate we use $N_{\mathrm{ngb}} = 20$ neighbours.

Once phase-space densities have been calculated, we sort the particles according to their density in descending order. Then we start to grow structures from high to low phase-space densities. While walking down in density we mark for each particle the two closest (according to the local phase-space metric) neighbours with higher phase-space density, if such particles exist. In this way we grow disjoint structures until we encounter a saddle point, which can be identified by observing the two marked particles and seeing if they belong to different structures. A saddle point occurs at the border of two structures. In the standard setup of HSF, which is used throughout this paper, the masses of the two structures separated by the saddle point are compared and the smaller one is cut, defining a complete individual structure. All particles below the saddle point whose higher density neighbours are part of the cut object are attached to the other, larger structure. Pursuing this procedure until all particles have been considered divides a halo into a unique disjoint set of substructures, of which the most massive, which also contains the lowest phase-density particles, is the main substructure.

When we wish to isolate self-bound subhaloes, we follow an identical procedure, except that each time we reach a saddle point, we remove all unbound particles iteratively from the smaller structure and attach them provisionally to the larger structure. Once we have followed this algorithm down to the lowest phase-density particle, we are left with a set of self-bound subhaloes and a few particles which are bound to no subhalo, not even the most massive self-bound subhalo which again is the one containing the lowest phase-density bound particles.

Both these procedures divide a halo into a disjoint set of phase-space structures, each containing a single phase-space density peak and bounded approximately by a level surface of phase-space density. In the first procedure each structure normally contains both bound and unbound particles, and all halo particles are assigned to some structure. In the second procedure, each structure is self-bound, and some halo particles are not assigned to any structure. To be specific, in the following we will refer to all particles inside r_{50}[1] as the *halo*. We call the most massive substructure constructed from these particles the *main halo*. Note that by definition it cannot extend beyond r_{50} and that its mean density within r_{50} will be less than 50 times the critical density. Note also that the main halo will change slightly according to whether we do or do not apply the unbinding and reassignment procedures. In the former case we refer to all other structures

---

[1] This is defined as the radius of the largest sphere centred on the halo density peak which encloses a mean density at least 50 times the critical value.

as (self-bound) *subhaloes*, whereas in the latter case we refer to them as *substructures*. A subhalo is thus always part of a substructure, but a substructure does not necessarily contain a subhalo.

3 STRUCTURES IN THE AQUARIUS SIMULATIONS

We study the phase-space structure of Milky Way-sized DM haloes using the high-resolution simulations of the Aquarius Project (Springel et al. 2008). The cosmological parameters for these simulations are $\Omega_m = 0.25, \Omega_\Lambda = 0.75, \sigma_8 = 0.9$ and $H_0 = 73 \mathrm{km\ s^{-1} Mpc^{-1}}$. For this project six Galaxy-mass haloes (Aq-A to Aq-F) were selected from a lower resolution version of the Millennium-II Simulation (Boylan-Kolchin et al. 2009) and resimulated with progressively higher particle number and smaller softening length. The haloes were selected to have no close massive companion at $z = 0$. When studying differences in phase-space structure between these haloes, we use the second resolution level (the highest for which results are available for all six objects). At this resolution all haloes have more than 1.6×10^8 particles inside r_{50}, corresponding to a particle mass $\sim 10^4 \mathrm{M_\odot}$. In addition, we use resimulations of the Aq-A halo at four different resolution levels to check the numerical convergence of our results. In the final section of this paper we investigate phase-space structure in the inner halo, defined as $r < r_{\mathrm{inner}} = 35$ kpc. For this purpose we use three resolution levels of the Aq-A halo with the largest one (Aq-A-1) having almost 1.5×10^9 particles inside r_{50} and more than 2×10^8 particles inside r_{inner}. Together with the ability of HSF to analyse the full 6D particle distribution, this simulation set allows the first robust and fully general quantification of the various phase-space components predicted by the ΛCDM model at $r \sim 8$ kpc where direct detection takes place.

3.1 A resolution study

We begin by analysing the mass functions of substructures and of self-bound subhaloes in the Aq-A halo and their dependence on resolution. To be consistent with earlier work we define the edge of the halo at $r_{50} = 433$ kpc and we count all objects within this radius, but we note that this is a large radius and, as a result, the counts are dominated by objects beyond 100 kpc, more than an order of magnitude further from the Galactic Centre than the Sun. In the upper panel of Fig. 1 we compare the differential mass functions of substructures (solid curves) and of self-bound subhaloes (dashed curves) at four different resolutions. The lower panel shows the corresponding cumulative mass functions. In both cases the mass functions agree quite well between the simulations above their respective resolution limits. For the self-bound subhaloes, the slope of the differential mass function is close to -1.9, as found earlier in the SUBFIND analysis of Springel et al. (2008). At lower resolution the distribution is better approximated, particularly in the low mass bins, by a slope close to -1.8. For the Aq-A-2 halo, we find that 14% of the halo mass is in self-bound subhaloes, which is 20% higher than the corresponding SUBFIND value (12%
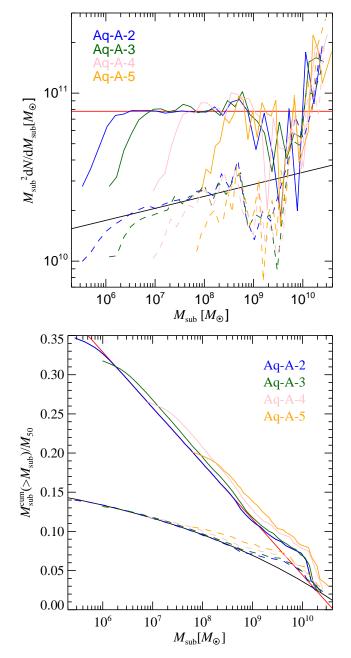

Figure 1. Top panel: Differential substructure mass functions for different resolutions of the Aq-A halo in the region $r < r_{50} = 433$ kpc. Solid lines indicate mass functions for the substructures identified when HSF is executed without unbinding and reassignment procedures (see the text), while dashed lines indicate the corresponding functions for the self-bound subhaloes found when these procedures are implemented. Different colours refer to the different resolution levels as indicated in the plot. The straight black line is a power-law fit, $\mathrm{d}N/\mathrm{d}M \propto M^{-1.9}$, to the data for self-bound subhaloes. The data for substructures are instead fit by a power-law of slope -2 (the horizontal red line). Bottom panel: Corresponding cumulative mass functions inside r_{50}, expressed as the total fraction of the enclosed mass in identified substructure. Line styles are the same as in the top panel. Black and red lines are based on the fits in the upper panel with a high mass truncation at 2% of the total mass.

- Springel et al. 2008), reflecting the fact that HSF typically attaches more mass to each identified object than SUBFIND. In the lower resolution simulations, particles from unresolved low-mass substructures are in many cases attached to more massive objects. This explains the shifts in the mass functions at high masses that are well resolved by all simulations (see the bottom panel of Fig.1). The mass fraction in self-bound subhaloes changes from 11% for Aq-A-5 to 14% for Aq-A-2.

The power-law behaviour of the mass function of self-bound subhaloes has been known for some time, but there has been controversy over its slope. If this slope is -2, then the mass fraction in subhaloes diverges logarithmically at low mass, and is cut off at a mass corresponding to the free-streaming length of the underlying DM particle (typically Earth mass for neutralino candidates). If the slope is -1.9, however, as found above, then the mass fraction in subhaloes has already effectively converged at the limit of the highest resolution Aquarius simulations and hence is $\sim 15\%$ within r_{50}. Within smaller radii this fraction drops dramatically, as we will see below.

HSF makes it possible to find unbound substructures also, and the solid lines in Fig. 1 show that within r_{50} rough numerical convergence is achieved for their mass function. In this case, however, the slope appears close to -2 and the mass in substructures exceeds that in self-bound subhaloes by more than a factor of 2 at all masses, and by increasingly large amounts at small mass. To the resolution limit of Aq-A-2, 35% of the mass within r_{50} is in substructure, showing the total mass detected in unbound tidal streams to be significantly larger than in self-bound subhaloes. With increasing resolution, significantly more substructures are found, and mass shifts from massive to smaller substructures, as found above for self-bound subhaloes but even more strongly. The behaviour seen in the lower panel of Fig. 1 cannot be extrapolated straightforwardly to lower mass. As we will see below, at the resolution of Aq-A-2, most of the mass in the outer halo is resolved into substructures, but relatively little of the mass in the inner regions. At higher resolution it will be the transition between these two regimes which controls the total mass fraction in substructure, rather than the increase in resolved substructures at any particular radius.

For this same resolution series of Aq-A simulations, Fig. 2 shows the mass fractions in substructures and in self-bound subhaloes for a set of of 10 disjoint spherical shells extending from 1 kpc to r_{50}. Within 35 kpc we also show results for the highest resolution simulation Aq-A-1. Although the results for a single simulation are rather noisy, they can be represented reasonably well by

$$f_{\rm sub}^{\rm loc} = \exp[\gamma + \beta \ln(r/r_{50}) + 0.5\alpha \ln^2(r/r_{50})], \quad (1)$$

with parameters $\alpha = -0.31, \beta = 0.98$ and $\gamma = -1.09$ for the subhaloes. This analytic form was used to fit the radial distribution of SUBFIND subhaloes in Springel et al. (2008). We note that the quoted parameters were obtained from a fit to data for the full set of six level 2 Aquarius haloes (see below). The distribution of HSF subhaloes is very similar to that of SUBFIND subhaloes, but HSF attaches slightly more particles to objects near the centre.

We find substructures down to 0.6 kpc in Aq-A-1 and down to 2 kpc in Aq-A-2 and Aq-A-3 simulations. For Aq-A-4, however, no substructures are found within ~ 9 kpc,
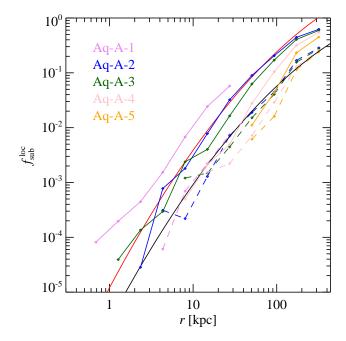

Figure 2. Fraction of mass in substructures and in self-bound subhaloes as a function of radius estimated from a set of disjoint spherical shells and for various resolution levels of the Aq-A halo as indicated by colour. We take the mass within r_{50} for the 4 lower resolution haloes. For Aq-A-1 only the mass within the inner 35 kpc was used. Solid lines represent the substructures and dashed lines the self-bound subhaloes. The black line is an analytic fit based on data for the full set of 6 Aquarius haloes (see below) $f_{\rm sub}^{\rm loc} = \exp[\gamma + \beta \ln(r/r_{50}) + 0.5\alpha \ln^2(r/r_{50})]$ with parameters $\alpha = -0.31, \beta = 0.98$ and $\gamma = -1.09$. The red line is the same function shifted vertically to $\gamma = 0.35$.

demonstrating that at least $\sim 10^7$ particles are needed within r_{50} to begin to study streams around the Sun's position. The red curve shows the prediction of Eq. (1) for parameters $\alpha = -0.31, \beta = 0.98$ and $\gamma = 0.35$ but, in contrast to the situation with subhaloes, it is clear that the results in the inner regions are not converging with increasing resolution. The results for Aq-A-1 lie well above the red line and should clearly still be considered as a lower limit to the mass fraction contained in tidal streams in these regions.

3.2   Mass distribution inside r_{50}

In this section we quantify the object-to-object scatter in the substructure mass function by analysing all six level 2 haloes of the Aquarius Project. Two of our haloes Aq-A and Aq-C did not experience major mergers below redshift 3. Haloes Aq-B and Aq-F on the other hand each underwent a major merger below redshift 1.5. More information on the merger history of the Aquarius haloes and how representative these haloes are of the population of Milky Way-like haloes can be found in Boylan-Kolchin et al. (2009) and in Wang et al. (2010).

The top panel of Fig. 3 shows the differential substructure mass function for the six Aquarius haloes Aq-A-2 to Aq-F-2; the bottom panel presents corresponding cumulative mass functions. Table 1 lists values for the total mass fraction in substructure in each halo using different substructure

Halo	SUBFIND (per cent)	N_{SUBFIND}	HSF subhaloes (per cent)	N_{HSF}	HSF substructures (per cent)
Aq-A-2	12.16	45024	14.14	48052	34.71
Aq-B-2	10.54	42537	14.44	44143	33.65
Aq-C-2	7.17	35022	7.72	36525	29.60
Aq-D-2	13.06	47014	14.26	49726	34.49
Aq-E-2	10.75	42725	13.10	44400	33.65
Aq-F-2	13.39	52503	15.16	57269	34.18

Table 1. Total mass in substructures within r_{50} for the 6 Aquarius haloes and different structure-finding methods. Mass fractions are calculated relative to the total mass within r_{50}. *Halo:* Aquarius halo label, *SUBFIND:* total mass fraction of particles in bound subhaloes found by SUBFIND; N_{SUBFIND}: number of bound subhaloes found by SUBFIND; *HSF subhaloes:* total mass fraction of particles in bound subhaloes found by HSF; N_{HSF}: number of bound subhaloes found by HSF; *HSF substructures:* total mass fraction of particles in substructures found by HSF.

identification methods. SUBFIND subhaloes (Springel et al. 2008) and subhaloes found by HSF follow the same power-law with a slope close to -1.9. Halo Aq-C-2 evolves in a quiet merger environment and this explains its deficit in substructures. For the general substructures the slope of the power-law is close to -2, but it is difficult to measure this value accurately because the low-mass end is contaminated by substructure arising through discreteness noise, particles which are connected by HSF but do not represent physical substructures.

In Aq-C-2 only 8% of the mass within r_{50} belongs to self-bound subhaloes, while for Aq-E-2 this number is 13% and for the other haloes it is $14 - 16\%$. The subhalo mass of Aq-F-2 is dominated by the largest subhaloes. It is interesting to observe that although Aq-C-2 has the fewest self-bound subhaloes, its mass fraction in substructures is about 30%, close to the value for Aq-B-2 (34%) which had completely different and much richer merger history. All the other haloes also have substructure mass fractions around 34%. The slope of the differential substructure mass function is similar in all haloes except Aq-F-2, where the very recent merger apparently causes a bias towards massive substructures.

Fig. 4 shows the fractions of mass in substructures (solid lines) and in self-bound subhaloes (dashed lines) as a function of distance from halo centre. For most of the haloes the latter follows Eq. (1), indicated as a black solid line. Clearly, HSF identifies substructures close to the centre in all halos. This is possible because of the high density contrast in 6D phase-space compared to 3D configuration space. Eq. (1) with a different normalisation (i.e. a vertical shift, see the solid black line) also gives a rough fit to the radial dependence of the substructure mass fraction in most haloes, but we note that an independent fit of the same functional form (the black dashed line) suggests that the mass fraction in substructures increases relative to that in self-bound subhaloes in the inner regions of the haloes.

In the outskirts of the haloes, near r_{50}, up to 30% of the mass is in the form of self-bound subhaloes and up to 60% resides in substructures.

4 THE INNER HALO

For many years experimenters have been trying to detect DM in laboratory devices. Detector signals are very sensi-

tive to the local DM phase-space distribution, so it is important to study halo structure in detail at the solar position. This requires high-resolution simulations like those of the Aquarius Project. A first phase-space analysis using the Aquarius haloes was carried out by Vogelsberger et al. (2009) with a focus on the local velocity and spatial distributions and their imprints on direct detection signals. Here we extend this study and focus on phase-space structures at $r \sim 8$ kpc. We go beyond the self-bound subhalo analysis of Springel et al. (2008) by using HSF, which efficiently identifies gravitationally unbound structures like tidal streams. Such features can have a significant impact on DM experiments, and our goal here is to quantify the total amount of structure in the inner halo, both bound and unbound. We therefore concentrate on the region within $r_{\mathrm{inner}} = 35$ kpc and use the excellent resolution of Aq-A-1 to analyse structures near the solar circle.

4.1 Substructure in the inner halo

To give a first impression of phase-space structure in the inner halo we use the technique of Maciejewski et al. (2009b). We estimate the phase-space density at the position of each particle with EnBiD (Sharma & Steinmetz 2006) and plot an r-v_r phase-space portrait in which each pixel is colour-coded according to the maximum phase-space density of the particles it contains. The top panel of Fig. 5 shows the resulting phase-space plot for the inner part of the Aq-A-2 halo, while the bottom panel shows the corresponding plot for Aq-A-1. Aq-A-2 has about 2.5×10^7 and Aq-A-1 about 2×10^8 particles inside r_{inner}. The increased resolution results in substantially more self-bound structures and tidal streams being visible in the inner regions of Aq-A-1. In the following we quantify these phase-space structures in some detail.

The solid lines in Fig. 6 show the differential mass functions of the substructures found by HSF within r_{inner} for the three highest resolution Aq-A haloes. The number of substructures more massive than $10^7 M_{\odot}$ is quite small and only for Aq-A-1 is the dynamic range sufficient to determine a power-law slope, which is close to -2. While the differential mass function for substructures within r_{50} (the top panel of Fig. 3) converges reasonably well with increasing resolution, this is not the case for the inner regions. Here, increasing resolution enables tidal streams to be followed to significantly lower contrast, substantially increasing the mass attached to
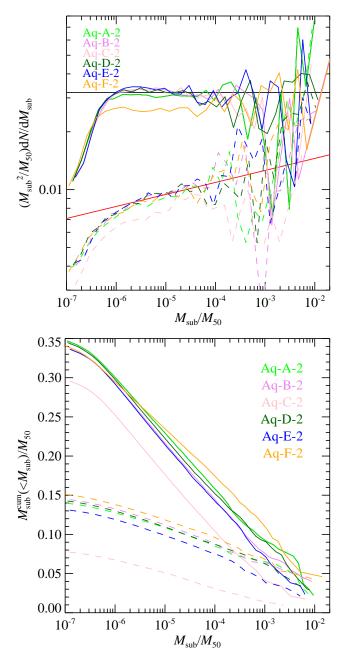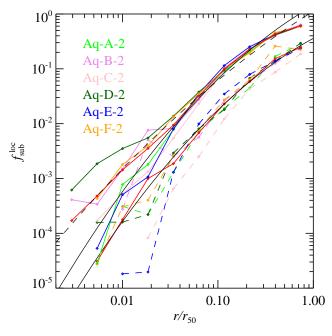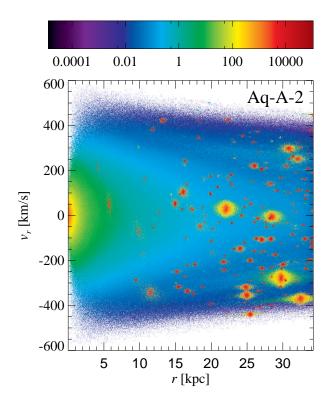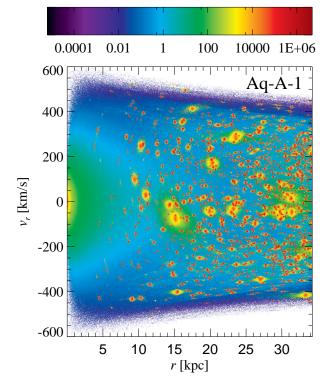
Figure 4. Fraction of mass in substructure as a function of radius for the six different haloes Aq-A-2 to Aq-F-2. Solid lines are for all substructures and dashed lines are for self-bound subhaloes. Red lines show the mean of the halo sample and black lines show analytic fits using the function $f_{\rm sub}^{\rm loc} = \exp[\gamma + \beta \ln(r/r_{50}) + 0.5\alpha \ln^2(r/r_{50})]$ with parameters $\alpha = -0.31, \beta = 0.98$ and $\gamma = -1.09$ for subhaloes and the same function shifted vertically to $\gamma = 0.35$ for substructures. The black dashed line shows the best fit for substructures with parameters $\alpha = -0.16, \beta = 1.10$ and $\gamma = 0.10$.

Figure 3. Top panel: Differential subhalo mass function for the six different Aquarius haloes Aq-A-2 to Aq-F-2. Solid lines show substructures and dashed lines self-bound subhaloes. The red line shows a power law $dN/dM \propto M^{-1.9}$ which is a good fit to the differential mass function of the self-bound subhaloes. The black line shows a -2 power-law which better describes the differential mass function of substructures. Bottom panel: The corresponding cumulative mass functions. Line styles are the same as in the top panel.

self-bound subhaloes. Although this number includes only subhaloes resolved in Aq-A-1, it is expected to increase by at most a factor of two if one extrapolates down to the free-streaming length (see Springel et al. 2008). The mass fraction in substructures in this same region increases from 0.82% for Aq-A-3 to 3.3% for Aq-A-1. Thus tidal streams contain almost 7 times as much mass as self-bound subhaloes at the resolution of Aq-A-1, and presumably would contain even more at higher resolution. As Fig. 4 shows, the substructure mass fraction varies as a function of radius. At the solar circle about 0.05% of the mass is in self-bound subhaloes and about 0.6% in tidal streams at the resolution of Aq-A-1. More than 99% of the mass appears smoothly distributed even at this extremely high resolution and when processed with a state-of-the-art 6D structure finder.

To give a visual impression of the structures found by HSF, Fig. 8 shows some typical substructures in the inner halo of Aq-A-1. The top panel presents the main halo with all HSF substructures (bound and unbound) removed. In the second row we show the biggest bound subhalo and its attached tidal streams. These extend over nearly 60 kpc. The mass of this biggest substructure is 2.9×10^8 M$_\odot$ of which 1.9×10^8 M$_\odot$ is in the self-bound subhalo. In the middle row we show an example of the same kind of substructure, but here the tidal tails are more pronounced and the stream passes within 8 kpc of halo centre. The bottom two rows show two typical stream-like structures which have no asso-
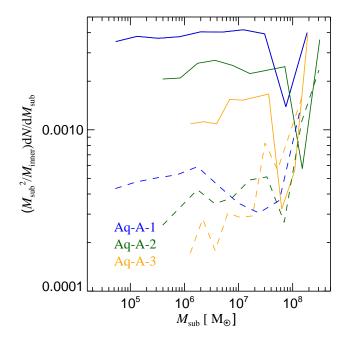
each one and so the total mass in substructures. This effect was already visible in Fig. 2 and is confirmed by the cumulative mass function shown in Fig. 7. Here also the curves for different resolutions agree much less well than was the case when we focused on substructures within r_{50} (see the bottom panel of Fig. 3).

Only 0.5% of the mass inside $r_{\rm inner}$ is in the form of

Figure 6. Differential mass functions for substructures and for self-bound subhaloes in the inner part of the Aq-A halo ($r < r_{\mathrm{inner}} = 35$ kpc) at various resolutions. Solid lines show results for substructures and dashed lines for self-bound subhaloes.
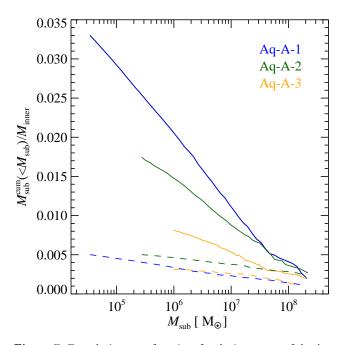

Figure 7. Cumulative mass functions for the inner part of the Aq-A halo ($r < r_{\mathrm{inner}} = 35$ kpc) at different resolutions. Solid lines represent substructures and dashed lines self-bound subhaloes. All curves are normalised to M_{inner}, the mass within r_{inner}.

Figure 5. Phase-space r-v_r plots of Aq-A-2 (top) and Aq-A-1 (bottom). These were constructed by first calculating the phase-space density at each particle using EnBiD (Sharma & Steinmetz 2006). We then create a pixelised image with 1000×1000 bins and for each pixel we calculate the logarithm of the maximum phase-space density over all particles in that pixel. The phase-space density is measured in units of $M_\odot$ kpc^{-3}km^{-3} s^3.

ciated self-bound subhalo. Their masses are similar to those of the biggest subhaloes.
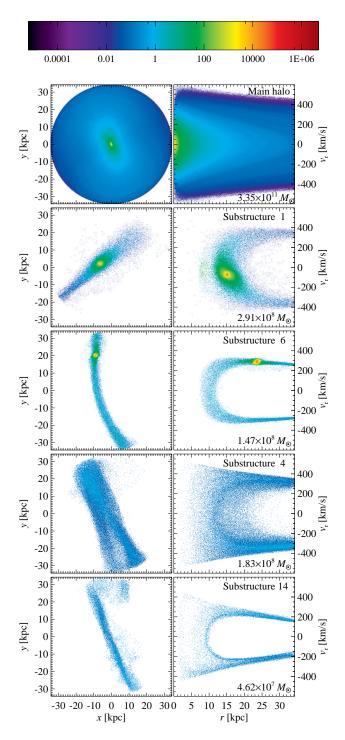
Figure 8. Plots of the main halo and some selected substructures in x-y and r-v_r projections for Aq-A-1. We create a 500×500 image and colour each pixel according to the logarithm of the maximum 6D phase-space density over the enclosed particles as estimated using EnBiD. The phase-space density is measured in units of $M_\odot$ kpc^{-3}km^{-3} s^3. The mass of each substructure is given in units of $M_\odot$ at the bottom right of each row.

4.2 Density probability distribution function

In this section we try to understand how the different components contribute to the dark matter density near the Sun. We ask how likely is it for the Solar System to lie within a subhalo or tidal stream of given local density. This is accomplished by computing probability density distributions for the space density at random points within a thick spherical shell centred at the Solar radius, as in Vogelsberger et al. (2009), but separating the dark matter into the different phase-space components identified by HSF. The result of this procedure is presented in Fig. 9.

The left panel of Fig. 9 shows the probability distribution function of DM density for various structures in the inner halo. To make this plot we first estimated the density at the position of every particle with radius between 6 and 12 kpc using a standard SPH scheme based on 32 neighbours. As described in Vogelsberger et al. (2009), we then fitted a smooth model to these values assuming the density to be stratified on similar, concentric ellipsoids and to be a power law of radius. This defines a model density $\rho_{\rm shell}$ at the position of each particle which can be compared with the directly estimated local density. This step is crucial to account for the large density gradients in the inner halo so that we can focus on small-scale variations due to substructure. We then repeat the SPH density estimates for the subsets of particles in this radial range corresponding to each individual subcomponent: the main subhalo and each individual self-bound subhalo and substructure. In the following we plot all density distributions as functions of $\rho/\rho_{\rm shell}$ and we construct volume-weighted probability distributions by histogramming the particles with individual weights $m_p/\rho V$, where m_p is the particle mass and V the total volume between 6 and 12 kpc. For the total mass distribution and the main subhalo the resulting distributions give the probability that an observer at a random point in this radial range will see local density contrast $\rho/\rho_{\rm shell}$. For the self-bound subhalo and substructure components, the distributions show the mean number of self-bound subhaloes or substructures with local density contrast $\rho/\rho_{\rm shell}$ at a random point.

If we consider first the probability distribution of density contrast for the total mass (i.e. the sum of all the components) we see that there is a lognormal distribution centred on $\rho/\rho_{\rm shell} = 1$ with an additional low amplitude, power-law tail to high densities. This result was already given in Vogelsberger et al. (2009). As they showed, the lognormal part of the distribution reflects discreteness noise in our density estimator. We demonstrate this again here by plotting as a dashed black line the distribution of analogous density estimates for points sampled from a uniform Poisson distribution. This line cannot be distinguished from that corresponding to the main subhalo in Fig. 9, demonstrating that this component follows our ellipsoidal model very closely. The power law tail is due to self-bound subhaloes, as is evident from its close agreement with the distribution calculated directly from this component. This general behaviour was pointed out not only in the analysis of this same simulation by Vogelsberger et al. (2009), but also in the analytic model of Kamionkowski & Koushiappas (2008) and in the analysis of a different high resolution simulation by Kamionkowski et. al. (2010).

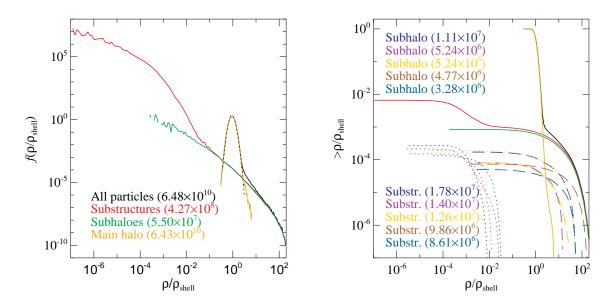If we now consider the density contrast distributions

Figure 9. *Left panel*: Volume-weighted density probability distributions for particles in the radial range $6-12$ kpc in Aq-A-1. For each particle an SPH-density is calculated using 32 neighbours. The resulting density field is fitted to a smooth ellipsoidal power-law model to obtain $\rho_{\rm shell}$. SPH-densities are also calculated using the particles in each individual subhalo and substructure separately; we do not consider individual subcomponents containing fewer than 64 particles. The results can be used to derive a density contrast $\rho/\rho_{\rm shell}$ at each particle's position, both in total mass and for the individual subcomponent to which the particle belongs. If V denotes the total volume between 6 and 12 kpc and m_p is the particle mass, then $m_p/\rho V$ is the probability that a random point in this radial range overlaps the particle. By histogramming this quantity for all particles we obtain the probability that a random point has density contrast $\rho/\rho_{\rm shell}$ (the black solid line). By instead histogramming this quantity for the particles in a single component using the ρ values calculated for individual subcomponents we obtain the mean number of subcomponents at a random position with local density contrast $\rho/\rho_{\rm shell}$ (yellow solid curve for the main subhalo, green for the set of self-bound subhaloes, red for the set of all substructures). Labels give the total mass in each component (in units of $M_\odot$). The black dashed line indicates the density contrast distribution produced by our density estimator for a Poisson realisation of a uniform density field. *Right panel*: Fraction of the mass in the radial range 6 to 12 kpc with density contrast above $\rho/\rho_{\rm shell}$ for all particles, for the main subhalo, for the self-bound subhalo population and for the substructure population. For the latter two, the density contrast is that of the individual object containing the particle. Colours are as in the left panel. This panel also shows cumulative mass fraction plots for the five most massive self-bound subhaloes (long-dashed lines) and for the five most massive substructures (dotted lines). The masses of the individual objects are given in parentheses (in units of $M_\odot$).

of the individual components, we see that self-bound subhaloes are detectable not only in the high-density tail but also down to contrasts as small as 10^{-4}. This reflects the excellent resolution of the Aq-A-1 simulation and, more importantly, the fact that our 6-D structure finder can identify subhalo material even at very low density contrast because of its small internal velocity dispersion. HSF identifies general phase-space substructure (e.g. tidal streams) down to even lower contrasts, of order 10^{-7}. The additional substructure mass which is not part of self-bound subhaloes is almost entirely in this low-contrast regime. It is interesting that the "probability" a random point lies in such a low-density tidal stream reaches values *much* larger than one, meaning that HSF has identified multiple structures at each point in 3-space. Note, however, that because low-density tidal streams have an effective spatial dimensionality less than 3, their $\rho/\rho_{\rm shell}$ values are biased low (and the mean stream number correspondingly high) by the spherical kernel of the SPH density estimator. In the radial range between 6 and 12 kpc selected for this analysis about 0.09% of the mass is in the form of self-bound subhaloes and about 0.7% in substructure. Thus low-density tidal streams account for almost 90% of the substructure detected by HSF.

The right panel of Fig. 9 shows, for the various compo-

nents, a cumulative plot of the mass at local density contrast exceeding $\rho/\rho_{\rm shell}$, expressed as a fraction of the total mass between 6 and 12 kpc. Here we see explicitly that the substructure component contains almost ten times as much mass as the bound subhalo component and that this excess lies almost exclusively at contrasts below 0.1. This panel also gives similar cumulative data for the five individually most massive self-bound subhaloes and for the five individually most massive substructures. Almost a third of the mass in self-bound subhaloes is contained in these five objects, almost all of it at density contrasts exceeding unity. However, only the most massive subhalo corresponds to one of the five most massive substructures, accounting for most of its mass. The other four massive substructures are unbound tidal streams with no associated subhalo. The maximum density contrast of these unbound streams is $\sim 10^{-2}$ (again this is probably biased low). The five most massive substructures together account for only about 10% of the total substructure mass.

4.3 Velocity distributions

Not only the mass density, but also the velocity distribution of DM particles in the vicinity of the Earth is relevant

for direct detection experiments. Vogelsberger et al. (2009) showed that although this velocity distribution is quite well approximated by a smooth trivariate Gaussian, potentially measurable features are imprinted on the corresponding energy distribution by the detailed formation history of the Milky Way's halo. Here we concentrate on the velocities of the different phase-space components in the inner halo. In Fig. 10 we show v_r-v_t projections of the distribution of all particles in the radial range 6 to 12 kpc (top), of those in substructures (middle), and of those in self-bound subhaloes (bottom). These plots are two-dimensional histograms, with colour encoding the mass in the corresponding bin as indicated by the colour bar (in units of solar masses per 2 km/s x 2 km/s pixel). The total mass contributing to each panel is given in its top right-hand corner. The main halo and so the bulk of the particles lie primarily at velocities below 200 km s^{-1}, whereas subhaloes and tidal streams are found almost exclusively at higher velocities. As a result, the most massive subhaloes are still (just) visible in the top panel despite the fact that they contribute less than a tenth of a percent of the mass. These structures contribute to the high-energy tail of the recoil spectrum in direct DM detection experiments, and so may be visible in high resolution experiments, particularly those with directional sensitivity which can detect the common motion of the substructure particles.

5   CONCLUSIONS

We study the population of subhaloes and tidal streams in six Milky Way-like DM haloes taken from the Aquarius Project. These structures are identified using the Hierarchical Structure Finder (HSF Maciejewski et al. 2009a), a state-of-the-art structure finder which operates in 6-D phase-space.

We find that that the differential mass function of self-bound subhaloes can be well described by a power-law with slope close to -1.9. This agrees with results from an independent analysis using the 3-D structure finder SUBFIND (Springel et al. 2008). Typically HSF attaches slightly more particles to subhaloes than SUBFIND, and also finds slightly more subhaloes above the simulation resolution limit (see Table 1). This agrees with previous results described in Maciejewski et al. (2009a). About 14% of the mass within r_{50} is in self-bound subhaloes, with significant scatter among the six haloes Aq-A to Aq-F. HSF subhalo masses are $\sim 10\%$ larger than those found by SUBFIND, although the increase can be larger near halo centre. In most haloes the total subhalo mass is dominated by the largest objects. The radial distributions of HSF and SUBFIND subhaloes are almost identical, although HSF can identify subhaloes closer to halo centre due to their enhanced density contrast in phase-space.

The differential mass function for substructures (i.e. both subhaloes and tidal streams) is also well described with a power-law, but in this case the slope is close to -2. This is independent of simulation resolution and holds approximately for all six haloes, thus appearing robust. For most of the level 2 haloes around 35% of the mass within r_{50} is assigned to substructures with mass above $\sim 3 \times 10^5 M_\odot$. The radial distribution of these objects can be approximated by equation (1) introduced in Springel et al. (2008) but with a
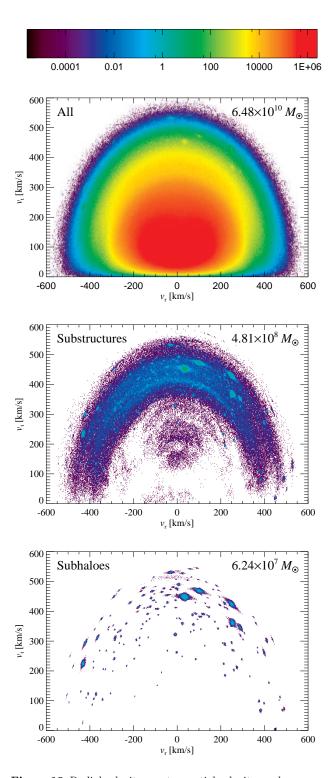

Figure 10. Radial velocity v_r – tangential velocity v_t phase-space plots for the $6 - 12$ kpc region of the Aq-A-1 halo. For each plot a two-dimensional histogram was calculated and colours were set to reflect the mass in each 2 km s^{-1} x 2 km s^{-1} pixel as shown by the colour bar, labelled in units of $M_\odot$. The top, middle and bottom panels show the distributions for all particles, for substructures and for subhaloes respectively. The low velocity region is dominated by the main halo but some substructures/subhaloes are still visible in the the high v_r and v_t velocity regions. HSF only detects significant substructure in these regions of phase-space. The total component mass in $M_\odot$ is indicated in the top right-hand corner of each panel.

higher normalisation than applies for self-bound subhaloes. In the inner halo almost 10 times as much mass is detected in unbound tidal streams as in self-bound subhaloes. This reflects the efficiency with which tidal forces destroy bound subhaloes in the inner halo.

In our highest resolution halo, Aq-A-1, HSF assigns about 0.5% of the mass within 35 kpc to self-bound subhaloes, and about 3.3% to substructures (subhaloes and tidal streams), with masses higher then $3 \times 10^4 M_\odot$. In this region the largest phase-space substructures are either self-bound subhaloes with massive tidal tails stretching across the entire inner 35 kpc region or equally massive tidal streams with no attached subhalo at $r < 35$ kpc. The largest individual substructures in the inner region have masses up to $3 \times 10^8 M_\odot$.

Vogelsberger et al. (2009) showed that the density field in the radial range from 6 to 12 kpc is very well represented by a simple smooth model where density is stratified on similar concentric ellipsoids and falls as a power law of radius. Fluctuations around this model are small except for a low-amplitude power-law tail to high density contrast which corresponds to self-bound subhaloes. Our HSF analysis is consistent with these results and allows us, in addition, to study the contrast of individual substructures with respect to the smooth background, the main subhalo, in which they are embedded. HSF is able to identify not only the high-contrast cores of individual self-bound subhaloes, but also their outskirts where the density contrast drops to values as low as $\sim 10^{-4}$. The maximum contrast of unbound tidal streams is $\sim 10^{-2}$. Since these streams contain 0.6% of the total mass between 6 and 12 kpc, of order one massive tidal stream is predicted to pass through every point, contributing a few tenths of a percent of the local DM density. In contrast, only 0.09% of the mass in this region is contributed by self-bound subhaloes, and the chance that the Earth lies in the high-density contrast region of such a subhalo is below 10^{-4}. Both subhaloes and tidal streams populate the high-energy tail of the velocity distribution preferentially, and would show up in direct DM detection experiments as a small but significant part of the signal in events with almost identical (vector) momenta.

REFERENCES

Aubert D., Pichon C., Colombi S., 2004, MNRAS, 352, 376
Boylan-Kolchin M., Springel V., White S. D. M., Jenkins A., 2010, MNRAS, 406, 896
Cole S., Lacey C., 1996, MNRAS, 281, 716
Davis M., Efstathiou G., Frenk C.S., White S.D.M., 1985, ApJ, 292, 371
Diemand J., Moore B., Stadel J., 2004, MNRAS, 352, 535
Diemand J., Moore B., Stadel J., 2005, Nature, 433, 389
Diemand J., Kuhlen M., Madau P., 2006, ApJ, 649, 1
Diemand J., Kuhlen M., Madau P., Zemp M., Moore B. et al., 2008, Nature, 454, 735
Ghigna S., Moore B., Governato F., Lake G., Quinn T. et al., 2000, ApJ, 544, 616
Governato F., Moore B., Cen R., Stadel J., Lake G., Quinn T., 1997, NewA, 2, 91
Kamionkowski M., Koushiappas S. M., 2008, Phys. Rev. D, 77, 103509
Kamionkowski M., Koushiappas S. M., Kuhlen M., 2010, Phys. Rev. D, 81, 043532
Kim J., Park, C., 2006, ApJ, 639, 600
Klypin A., Kravtsov A. V., Valenzuela O., Prada F., 1999, ApJ, 522, 82
Knollmann S. R., Knebe A., ApJS, 2009, 182, 608
Maciejewski M., Colombi S., Springel V., Alard C., Bouchet F. R., 2009a, MNRAS, 396, 1329
Maciejewski M., Colombi S., Alard C., Bouchet F., Pichon C., 2009b, MNRAS, 393, 703
Moore B., Ghigna S., Governato F., Lake G., Quinn T. et al., 1999, ApJ, 524, L19
Neyrinck M. C., Gnedin N. Y., Hamilton A. J. S., 2005, MNRAS, 356, 1222
Sharma S., Steinmetz M., 2006, MNRAS 373, 1293
Sharma S., Johnston K.V., 2009, ApJ, 703, 1061
Springel V., White S. D. M., Tormen G., Kauffmann G., 2001, MNRAS, 328, 726
Springel V., Wang J., Vogelsberger M., Ludlow A., Jenkins A. et al., 2008, MNRAS, 391, 1685
Stoehr F., White S. D. M., Tormen G., Springel V., 2002, MNRAS, 335, 84
Vogelsberger M., Amina H., Springel V., White S. D. M., Wang J. et al., 2009, MNRAS, 395, 797
Vogelsberger M., White S. D .M., 2010, arXiv:1002.3162
Wang J., Navarro J. F., Frenk C. S., White S. D. M., Springel V. et al., 2010, arXiv:1008.5114